

# Gravitational Lensing Effects by Galaxy Clusters on Ionised Bubble Size Distribution during the Epoch of Reionisation

Di Wu,<sup>1,2</sup> Nan Li,<sup>1,2,3\*</sup> Huanyuan Shan<sup>4,5†</sup> and Zhenghao Zhu<sup>4</sup>

<sup>1</sup>National Astronomical Observatories, Chinese Academy of Sciences, 20A Datun Road, Chaoyang District, Beijing 100101, China

<sup>2</sup>School of Astronomy and Space Science, University of Chinese Academy of Sciences, Beijing 100049, China

<sup>3</sup>Key Laboratory of Space Astronomy and Technology, National Astronomical Observatories, Chinese Academy of Sciences, 20A Datun Road, Chaoyang District, Beijing 100101, China

<sup>4</sup>Shanghai Astronomical Observatory, Chinese Academy of Sciences, 80 Nandan Road, Shanghai 200030, China

<sup>5</sup>State Key Laboratory of Radio Astronomy and Technology, A20 Datun Road, Chaoyang District, Beijing, 100101, P. R. China

Accepted XXX. Received YYY; in original form ZZZ

## ABSTRACT

The statistical properties of ionisation structures during the Epoch of Reionisation (EoR) provide valuable insights into the formation of the first stars and galaxies. However, statistics such as size distributions of ionisation structures can be affected by gravitational lensing caused by foreground massive structures like galaxy clusters. Hence, to quantify the impacts of lensing by galaxy clusters on ionised Bubble Size Distribution (BSD), we conducted a series of multiple-lens-plane lensing simulations involving the light cones of clusters alongside source light cones based on various ionisation models. The deflector population is generated using the Monte Carlo method, guided by halo mass function and empirical scaling relations, while deflectors' mass profile is modelled using the Truncated Navarro-Frenk-White (TNFW) model. Source light cones are produced via a semi-numerical approach or directly sourced from the Evolution of 21 cm Structure (EOS) project. By employing the Mean Free Path method, we measure unlensed and lensed BSD to reveal the lensing impacts. Our results indicate that lensing effects increase the number of large bubbles while leaving the number of small bubbles unchanged across all source models we adopted. Specifically, for the EOS faint galaxies model, the number of  $R > 15$  cMpc bubbles increases by 219% at  $z = 14$ ; for the EOS bright galaxies model, the above number increases by 832% under the same circumstances. Above all, lensing introduces unavoidable systematics for BSD, which must be carefully taken into account for relevant studies in the Square Kilometre Array (SKA) era.

**Key words:** cosmology: dark ages, reionization, first stars – galaxies: clusters: general – gravitational lensing: strong – gravitational lensing: weak – galaxies: intergalactic medium

## 1 INTRODUCTION

The Epoch of Reionisation (EoR) is a pivotal period in the history of cosmic evolution, during which the universe underwent a global phase transition, shifting from a completely neutral state to one that is almost entirely ionised (Ciardi & Ferrara 2005; Furlanetto et al. 2006; Morales & Wyithe 2010; Pritchard & Loeb 2012; Stark 2016; Dayal 2019; Liu & Shaw 2020). Observations and theoretical studies of the EoR are beneficial in understanding the properties of the first generation of stars (Yoshida et al. 2006; Xu et al. 2016; Katz et al. 2023; Venditti et al. 2024) and galaxies (Mao et al. 2008; Naoz & Barkana 2008; Watson et al. 2015; Jones et al. 2024) in the Universe, comprehending the formation of large-scale cosmic structures (Silva et al. 2021), and constraining cosmological models (McQuinn et al. 2006; Mao et al. 2008; Castellano et al. 2023; Dayal & Giri 2024).

Ionised bubbles are ionised regions in the intergalactic medium (IGM) during the EoR, which appear as dark areas in the 21 cm

signal images of neutral hydrogen. The Bubble Size Distribution (BSD) represents the topology of reionisation (Lin et al. 2016) and is one of the most important tracers for probing the progress of cosmic reionisation (Wyithe & Loeb 2004; Tilvi et al. 2020a). A large number of theoretical investigations have indicated that ionised bubbles form around ionising sources and grow in isolation in the initial stage, and as reionisation proceeds, different ionised bubbles merge, eventually leading to the complete ionisation of the IGM (Zahn et al. 2007; Mesinger & Furlanetto 2007; Furlanetto & Oh 2016; Qin et al. 2022; Lu et al. 2024). Therefore, the evolution of BSD along redshift characterises the progress of reionisation, which is a powerful tool to constrain the parameters of reionisation models by comparing observations with theoretical predictions (McQuinn et al. 2007; Tashiro & Sugiyama 2012; Doussot & Semelin 2022; Lu et al. 2024).

Among the tracers utilised to determine the properties of ionised bubbles during the EoR, the Lyman- $\alpha$  emission by high-redshift galaxies (Malhotra & Rhoads 2006; Dijkstra 2014; Mason et al. 2018) and the 21 cm signal in the radio band (Datta et al. 2007; Giri et al. 2018; Shimabukuro et al. 2022; Mishra et al. 2024) are

\* E-mail: nan.li@nao.cas.cn (NL)

† E-mail: hyshan@shao.ac.cn (HS)

two notable representatives. The Lyman- $\alpha$  emission by high-redshift galaxies serves as an indirect tracer for inferring the morphology and size of ionised bubbles (Endsley & Stark 2022; Trapp et al. 2023; Castellano et al. 2016, 2018; Tilvi et al. 2020b; Larson et al. 2022; Tang et al. 2023), as it is significantly attenuated by neutral hydrogen regions in the intergalactic medium (IGM), while ionised hydrogen regions do not absorb it. The direct tracer for assessing the morphology and size of ionised bubbles is the 21 cm emission from hydrogen itself in the radio band. Although the detection of the 21 cm emission from the EoR is challenging due to weak signals and considerable foreground contamination, plenty of efforts continue to advance this field, such as the Murchison Widefield Array (MWA)<sup>1</sup> (Tingay et al. 2013), the 21 CentiMeter Array (21CMA)<sup>2</sup> (Zheng et al. 2016), the Low-Frequency Array (LOFAR)<sup>3</sup> (van Haarlem et al. 2013), the Hydrogen Epoch of Reionization Array (HERA)<sup>4</sup> (DeBoer et al. 2017), and the Precision Array for Probing the Epoch of Reionization (PAPER)<sup>5</sup> (Parsons et al. 2010). To date, the upper limit of the 21 cm signal power spectrum during the EoR has been explored extensively (Barry et al. 2019; Mertens et al. 2020; Yoshiura et al. 2021; Abdurashidova et al. 2022; Kolopanis et al. 2019), and the next-generation radio interferometer arrays like the Square Kilometre Array (SKA) are anticipated to directly observe the 21 cm signal from the EoR (Mellema et al. 2015).

Gravitational lensing distorts the morphology of background sources due to the deflection of light (Schneider et al. 1992; Narayan & Bartelmann 1996; Wambsganss 1998; Bartelmann 2010; Saha et al. 2024). An effect which is known as magnification bias (Turner 1980; Borgeest et al. 1991; Schneider et al. 1992; Wyithe 2004; von Wietersheim Kramsta et al. 2021), refers to the resulting selection bias caused by the lensing effect in flux- or size-limited samples, affecting the size or morphology distributions of high-redshift objects. For instance, the luminosity function of submillimeter galaxies, which are primarily distributed at redshifts 1 to 4, shows an observed number density at the bright end that is much higher than the theoretical predictions due to the lensing effects (Blain 1996; Lima et al. 2010; Er et al. 2013). Similarly, the number density of bright UV galaxies at redshift around 8 has been significantly enhanced by gravitational lensing (Mason et al. 2015). Therefore, when utilising the BSD to infer the progress of reionisation and constrain the parameters of reionisation models, ignoring lensing effects may lead to systematic bias. Consequently, quantifying this impact is necessary, but it is still unclear.

In this paper, to quantify the gravitational lensing effects on BSD by clusters thoroughly, we conducted a series of multiple-lens-plane lensing simulations involving a light cone of clusters alongside source light cones based on various ionisation models. Expressly, the deflector population is generated using the Monte Carlo method, guided by the halo mass function (Tinker et al. 2008) which describes the halo density at different masses and redshifts, while the deflectors' mass profile is modelled using the Truncated Navarro-Frenk-White (TNFW) model (Navarro et al. 1997; Baltz et al. 2009). To explore the influences of lensing on BSD for different ionisation simulation models, we produce three types of source light cones via a semi-numerical approach by using Python package 21CMFAST v3 (Mesinger et al. 2016; Murray et al. 2020), at the same time two

source light cones from the Evolution of 21 cm Structure (EOS) project (Mesinger et al. 2016) are adopted. Subsequently, we run multi-lens-plane ray-tracing lensing simulations with the above mass and source light cones to generate two-dimensional (2D)  $x_{\text{HI}}$  (neutral hydrogen fraction) maps with lensing effects. Following this, by comparing the BSDs, measured with the Mean Free Path (MFP) method (Mesinger & Furlanetto 2007), and their evolution along redshift from the 2D  $x_{\text{HI}}$  maps with and without lensing effects, impacts of lensing on BSD can be quantified. Our findings reveal that the impacts of lensing are noteworthy on larger ionised bubbles at the early stage of EoR when redshift  $\sim 12 - 14$  across all source models adopted, necessitating careful consideration in studies related to BSD in the era of the SKA.

The structure of this paper is as follows. Sect. 2 introduces the basics of reionisation and gravitational lensing relevant to this work. In Sect. 3, we detail the implementation of our simulations. Sect. 4 describes the algorithm used to measure the BSD, and Sect. 5 presents our findings. Lastly, we draw conclusions in Sect. 6. Throughout this study, we adopt the  $\Lambda$ CDM cosmology, unless otherwise specified, the cosmological parameters are set based on the results from Planck 2018 (Planck Collaboration et al. 2020):  $\Omega_{\Lambda} = 0.6889$ ,  $\Omega_{\text{m}} = 0.3111$ ,  $\Omega_{\text{b}} = 0.04897$ ,  $n_{\text{s}} = 0.9665$ , and  $H_0 = 67.66 \text{ km s}^{-1} \text{ Mpc}^{-1}$ .

## 2 THEORY

In this section, we review the basic theory of the EoR and of gravitational lensing in Sect. 2.1 and Sect. 2.2, respectively.

### 2.1 Basics of EoR simulation

The EoR simulations used in this work were generated with the publicly available Python software 21CMFAST (Mesinger et al. 2011, 2016; Murray et al. 2020). 21CMFAST employs a semi-numerical approach to model the evolution of key parameters during the EoR. In particular, the code simulates the 21 cm differential brightness temperature  $\delta T_b(\nu)$  as given by Furlanetto et al. (2006):

$$\delta T_b(\nu) \approx 27 x_{\text{HI}} (1 + \delta_{\text{nl}}) \left( \frac{H(z)}{dv_r/dr + H(z)} \right) \left( 1 - \frac{T_{\gamma}}{T_s} \right) \times \left( \frac{1+z}{10} \frac{0.15}{\Omega_{\text{m}} h^2} \right)^{1/2} \left( \frac{\Omega_{\text{b}} h^2}{0.023} \right) \text{mK}, \quad (1)$$

where  $T_s$  is the spin temperature of the neutral hydrogen gas, and  $T_{\gamma}$  denotes the CMB photon temperature. We simulate the evolution of  $T_s$  and  $T_{\gamma}$  in this work instead of assuming the saturation of  $T_s$ . The quantity  $\delta_{\text{nl}}(\mathbf{x}, z) \equiv \rho/\bar{\rho} - 1$  is the density contrast;  $H(z)$  is the Hubble parameter;  $dv_r/dr$  is the comoving line-of-sight velocity gradient; and  $z$  is the redshift.

The  $x_{\text{HI}}$  is determined by the ionising influence of sources on their surrounding environment. This is modelled using an excursion-set formalism (Furlanetto et al. 2004; Mesinger et al. 2016), in which a cell is considered ionised if it satisfies the criterion:

$$\zeta f_{\text{coll}}(\mathbf{x}, z, R, M_{\text{min}}) \geq 1 + \bar{n}_{\text{rec}}(\mathbf{x}, z, R). \quad (2)$$

Here  $f_{\text{coll}}(\mathbf{x}, z, R, M_{\text{min}})$  is the fraction of collapsed matter inside a spherical region of radius  $R$  (centred at position  $\mathbf{x}$ ),  $\bar{n}_{\text{rec}}(\mathbf{x}, z, R)$  is the cumulative number of recombinations (Sobacchi & Mesinger 2014), and  $\zeta$  is the ionising efficiency (treated as a free parameter) (Greig & Mesinger 2015). This excursion-set method effectively accounts for ionising photons from all sources hosted in haloes above the mass threshold  $M_{\text{min}}$ .

<sup>1</sup> MWA, <http://www.mwatelescope.org>

<sup>2</sup> 21CMA, [https://english.nao.cas.cn/Research2015/rp2015/201701/t20170120\\_173603.html](https://english.nao.cas.cn/Research2015/rp2015/201701/t20170120_173603.html)

<sup>3</sup> LOFAR, <http://www.lofar.org>

<sup>4</sup> HERA, <https://reionization.org/>

<sup>5</sup> PAPER, <http://eor.berkeley.edu>

The parameter  $M_{\min}$  represents the minimum halo mass capable of hosting ionising sources. It is often defined via the halo's virial temperature (i.e. the atomic cooling threshold). The relation between halo mass  $M_{\text{halo}}$  and virial temperature  $T_{\text{vir}}$  is given by [Barkana & Loeb \(2001\)](#):

$$M_{\text{halo}} = 10^8 h^{-1} \left( \frac{w}{0.6} \right)^{-3/2} \left( \frac{\Omega_m}{\Omega_m^z} \frac{\Delta_c}{18\pi^2} \right)^{-1/2} \times \left( \frac{T_{\text{vir}}}{1.98 \times 10^4 \text{ K}} \right)^{3/2} \left( \frac{1+z}{10} \right)^{-3/2} M_{\odot}. \quad (3)$$

Here  $\Omega_m^z \equiv \frac{\Omega_m(1+z)^3}{\Omega_m(1+z)^3 + \Omega_{\Lambda}}$  is the effective matter density fraction at redshift  $z$ ,  $w$  is the mean molecular weight, and the collapse overdensity is  $\Delta_c = 18\pi^2 + 82d - 39d^2$  with  $d \equiv \Omega_m^z - 1$ . Both  $M_{\min}$  and  $\zeta$  are crucial parameters for modelling the reionisation process. We discuss their impact on our simulations in Sect. 3.

## 2.2 Basics of Gravitational Lensing

We adopt the thin-lens approximation for the calculation of gravitational lensing ([Schneider et al. 1992](#)) in this paper, and the dimensionless projected surface mass density of the lens (the convergence) is given by:

$$\kappa(\boldsymbol{\theta}) = \frac{\Sigma(\boldsymbol{\theta})}{\Sigma_{\text{cr}}}, \quad (4)$$

where  $\Sigma_{\text{cr}}$  is the critical surface mass density given by:

$$\Sigma_{\text{cr}} = \frac{c^2}{4\pi G} \frac{D_s}{D_d D_{ds}}. \quad (5)$$

Here  $D_s$ ,  $D_d$ , and  $D_{ds}$  are the angular diameter distances from the observer to the source plane, from the observer to the lens plane, and from the lens plane to the source plane, respectively.  $\Sigma(\boldsymbol{\theta})$  is the physical surface mass density of the lens,  $c$  is the speed of light, and  $G$  is the gravitational constant. The lensing potential  $\psi(\boldsymbol{\theta})$  is defined by:

$$\psi(\boldsymbol{\theta}) = \frac{1}{\pi} \int_{\mathbb{R}^2} \kappa(\boldsymbol{\theta}') \ln |\boldsymbol{\theta} - \boldsymbol{\theta}'| d^2 \theta', \quad (6)$$

From this potential, one can derive the standard lensing quantities. For example, the (reduced) deflection angle is given by

$$\boldsymbol{\alpha}(\boldsymbol{\theta}) = \nabla \psi(\boldsymbol{\theta}). \quad (7)$$

The relationship between the source position  $\boldsymbol{\beta}$  and the image position  $\boldsymbol{\theta}$  is given by the lensing equation:

$$\boldsymbol{\beta} = \boldsymbol{\theta} - \boldsymbol{\alpha}(\boldsymbol{\theta}). \quad (8)$$

This work employs the multiple-lens-plane ray-tracing approach. Specifically,  $\kappa$  at position  $\boldsymbol{\theta}_i$  on the  $i$ th lens plane can be expressed by the following formula in ([Schneider et al. 1992](#)):

$$\kappa_i(\boldsymbol{\theta}_i) = \frac{4\pi G}{c^2} \frac{D_i D_{is}}{D_s} \Sigma_i(D_i \boldsymbol{\theta}_i), \quad (9)$$

where  $D_i$  and  $D_{is}$  are the angular diameter distance from the observer to the  $i$ th lens plane and from the  $i$ th lens plane to the source plane, respectively.  $\Sigma_i(D_i \boldsymbol{\theta}_i)$  is the surface mass density at  $D_i \boldsymbol{\theta}_i$ . Using Eq. (6) and Eq. (7), one can get the deflection angle  $\boldsymbol{\alpha}(\boldsymbol{\theta}_i)$  on the  $i$ th lens plane. Thus, the lensing equation Eq. (8) becomes

$$\boldsymbol{\theta}_j = \boldsymbol{\theta}_1 - \sum_{i=1}^{j-1} \frac{D_{ij} D_s}{D_j D_{is}} \boldsymbol{\alpha}(\boldsymbol{\theta}_i), \quad (10)$$

where  $\boldsymbol{\theta}_j$  is the angular position of the light ray on the  $j$ th lens plane,  $D_j$  and  $D_{ij}$  are the angular diameter distance from observer to  $j$ th lens plane and from  $i$ th lens plane to  $j$ th lens plane.

## 3 SIMULATIONS

This section comprehensively explains our simulations to generate lensed EoR maps to quantify the lensing effects on BSDs. Sect. 3.1 details the generation of the reionisation simulations. Sect. 3.2 describes the construction of the light cones of deflectors. At last, Sect. 3.3 presents the implementation of the lensing simulations based on the above two components.

### 3.1 EoR simulations

This study utilises five distinct reionisation simulations to systematically investigate the effects of ionisation parameter settings and simulation resolution. The selection of multiple simulations is motivated by two key considerations: one is the current lack of well-constrained ionisation parameters, and another is the need to explore resolution-dependent effects in ionisation simulations. Among the five simulations, two are adopted from the EOS project data release ([Mesinger et al. 2016](#)), specifically the Faint Galaxies and Bright Galaxies models. To complement these established models, we have developed three additional simulations with varying resolutions, designated as LOW-RES (low resolution), MID-RES (medium resolution), and HIGH-RES (high resolution), which were produced by 21CMFAST v3 ([Mesinger et al. 2016](#); [Murray et al. 2020](#)). The complete specifications of all simulations are provided in Table 1. We note that the EoR simulations used in this work assume that foregrounds are perfectly removed.

We employ two contrasting reionisation models from the EOS project: the Faint Galaxies model and the Bright Galaxies model. These complementary approaches enable systematic investigation of ionisation model dependencies in gravitational lensing effects, handling the unresolved debate concerning the relative contributions of faint and bright galaxies to reionisation processes ([Finkelstein et al. 2019](#); [Naidu et al. 2020](#)). In the Faint Galaxies model, ionisation sources are dominated by small haloes near the atomic cooling threshold of  $T_{\text{vir}} = 2 \times 10^4 \text{ K}$ , with an ionising efficiency of  $\zeta = 20$ . Conversely, the Bright Galaxies model implements an elevated virial temperature threshold  $T_{\text{vir}} = 2 \times 10^5 \text{ K}$  to account for suppressed star formation in low-mass haloes through efficient supernova feedback mechanisms, while adopting a significantly enhanced ionising efficiency of  $\zeta = 200$ . These simulations are processed into two light cones, each with a field of view of  $2.5^\circ \times 2.5^\circ$ . Cosmological parameters used in these two EOS simulations are from the Planck 2015 ([Planck Collaboration et al. 2016](#)), which are slightly different from the Planck 2018 Cosmological parameters adopted in other parts of the simulations in this work.

To systematically evaluate resolution-dependent effects in our analysis, we performed three additional ionisation simulations using the public semi-numerical code 21CMFAST v3 ([Murray et al. 2020](#)): LOW-RES, MID-RES, and HIGH-RES. These simulations share identical ionisation parameters ( $\zeta = 30$ ,  $T_{\text{vir}} = 5 \times 10^4 \text{ K}$ ) but employ progressively refined spatial resolutions: the  $(125 \text{ cMpc})^3$  volume with initial density grids of  $192^3$ ,  $384^3$ , and  $768^3$  voxels, subsequently smoothed down to ionisation maps with  $64^3$ ,  $128^3$ , and  $256^3$  grids having cell sizes of approximately 2, 1, and 0.5 cMpc respectively. For each resolution configuration, we generated sixteen  $0.625^\circ \times 0.625^\circ$  independent light cones using distinct initial density fields to mitigate sample noise from cosmic variance. As an illustration, Figure 1 shows a slice of one HIGH-RES light cone. For the simulation prescription, all three models are generated using 21CMFAST v3 with inhomogeneous recombinations ([Sobacchi](#)

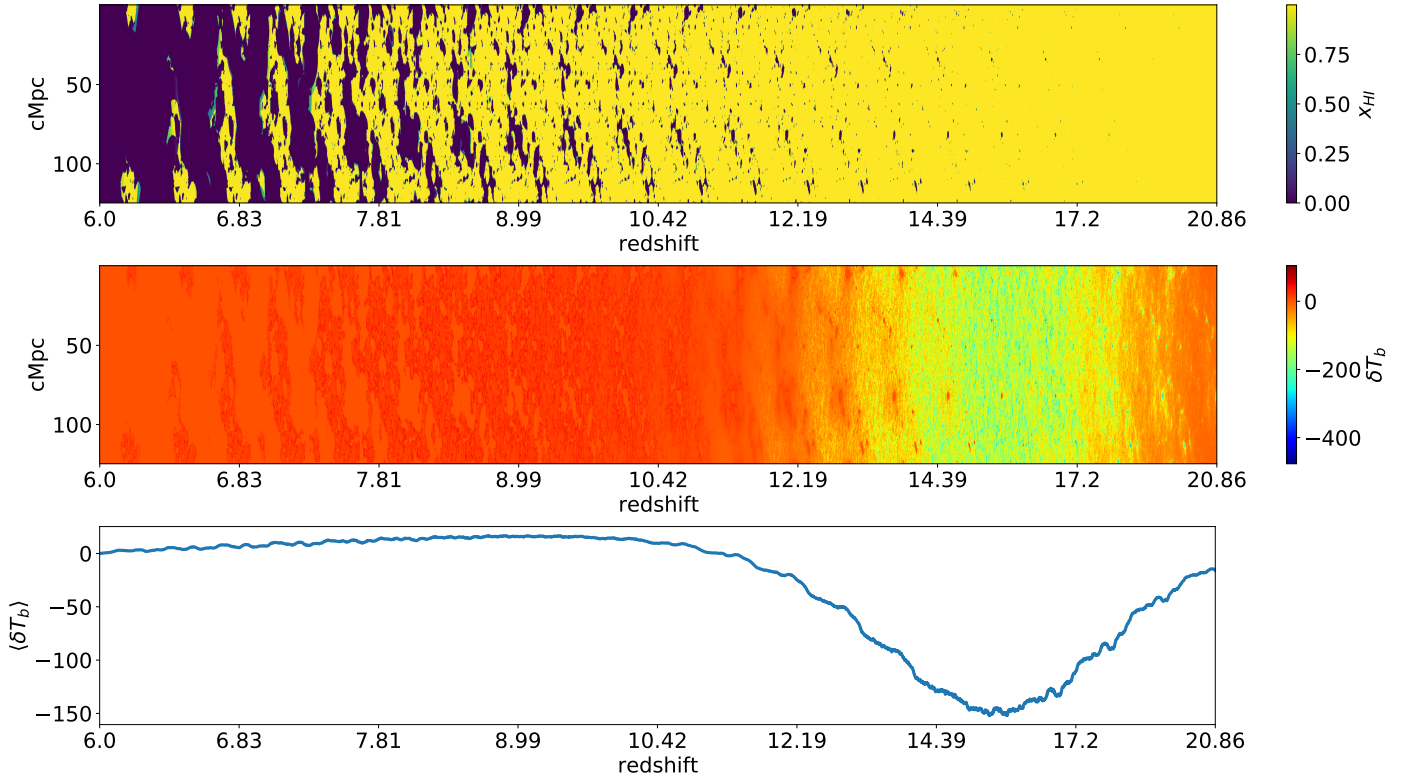


**Figure 1.** Demonstration of a slice in the redshift direction of one HIGH-RES simulation. The upper panel shows the evolution of the  $x_{\text{HI}}$  (neutral hydrogen fraction). The middle panel displays the 21 cm differential brightness temperature. The lower panel presents the global 21 cm differential brightness temperature evolution.

**Table 1.** Parameter descriptions of ionisation simulations.

Name	ionisation simulation resolution (cMpc)	Number of light cones $\times$ (field of view)	$\zeta$	$T_{\text{vir}} (M_{\text{min}})$ (K)
Faint galaxies model	1.5625	$1 \times (2.5^\circ \times 2.5^\circ)$	20	$2 \times 10^4$
Bright galaxies model	1.5625	$1 \times (2.5^\circ \times 2.5^\circ)$	200	$2 \times 10^5$
LOW-RES	2	$16 \times (0.625^\circ \times 0.625^\circ)$	30	$5 \times 10^4$
MID-RES	1	$16 \times (0.625^\circ \times 0.625^\circ)$	30	$5 \times 10^4$
HIGH-RES	0.5	$16 \times (0.625^\circ \times 0.625^\circ)$	30	$5 \times 10^4$

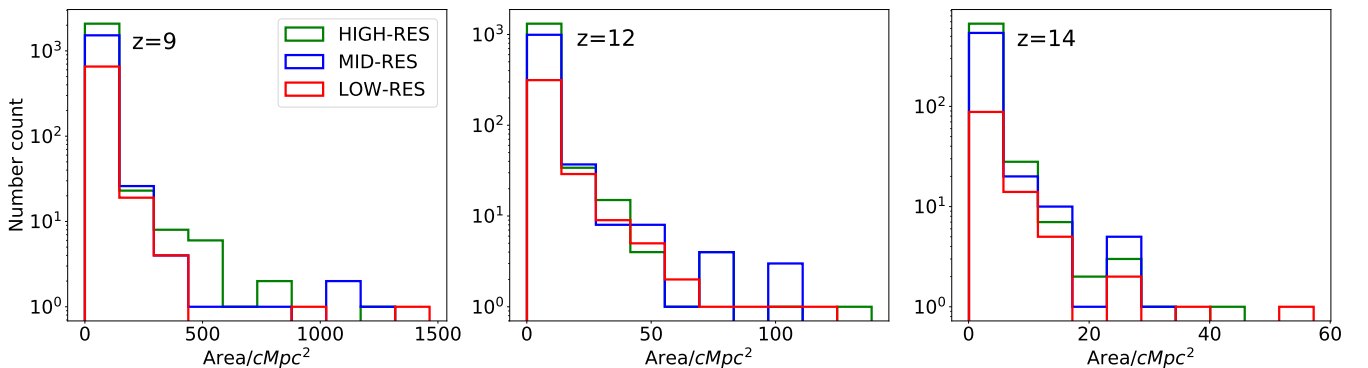


**Figure 2.** Number counts of ionised bubbles as a function of projected area of bubble for simulation slices at redshifts  $z=9$  (left),  $z=12$  (middle), and  $z=14$  (right), respectively. Bubbles were identified via a Friends-of-Friends (FoF) algorithm (Iliev et al. 2006) using an ionisation fraction threshold of 0.5. The HIGH-RES resolves the highest abundance of small-scale ionised regions across all three epochs, highlighting the impact of spatial resolution on the recovered small-scale ionisation topology.

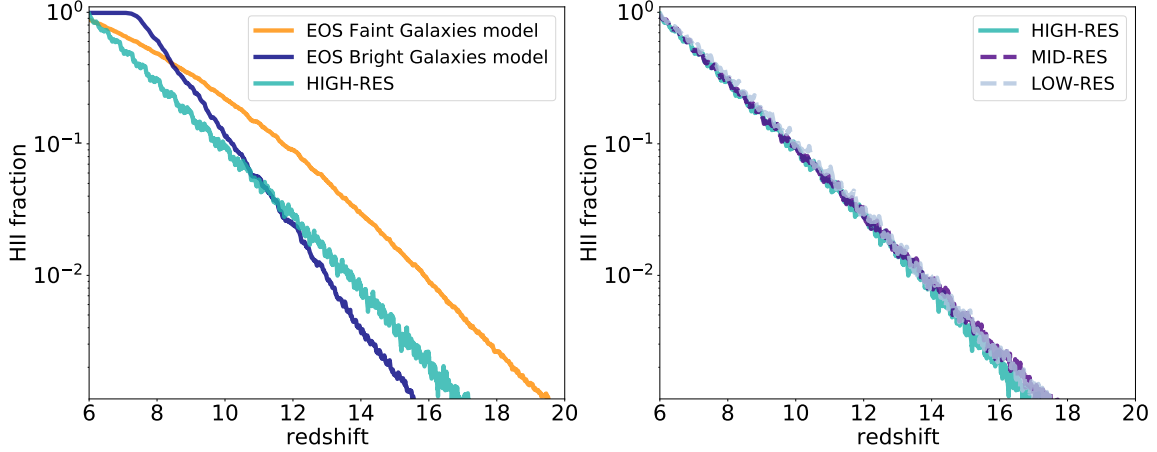


**Figure 3.** Global volume-averaged HII (ionised hydrogen) fraction evolutions for the five ionisation models (listed in Table 1) used in this work. **Left:** Ionised fraction evolution for three ionisation models with different ionisation parameter settings: EOS Faint Galaxies model, EOS Bright Galaxies model, and HIGH-RES. **Right:** Ionised fraction evolution for three models with the same ionisation parameter settings but different resolution settings: HIGH-RES, MID-RES, and LOW-RES. The different colours represent different models. Left panel shows that simulations with different parameter settings exhibit distinct ionisation processes, such as variations in the reionisation redshift range and the speed of ionisation. Conversely, the right panel shows that simulations with the same ionisation parameter settings ( $\zeta$  and  $M_{\min}$ ) have similar reionisation processes, despite differences in ionisation simulation resolution.

& Mesinger 2014) enabled and without assuming a saturated spin temperature.

Our analysis reveals a resolution dependence in the characterisation of small-scale ionised bubbles across the LOW-RES, MID-RES, and HIGH-RES simulation suites. Comparison of ionised bubble counts in 2D slices at redshifts  $z = 9$ ,  $z = 12$ , and  $z = 14$  is shown in Figure 2, which demonstrates that higher spatial resolution enables the presence of significantly more small-scale ionised regions. Here we employ the Friends-of-Friends (FoF) algorithm (Iliev et al. 2006) using the Tools21cm package (Giri et al. 2020) for bubble identification, which provides one important methodological advantage for comparison that it directly shows the number of ionised bubbles in each size bin. The linking length of the FoF algorithm is set to the size of the corresponding original reionisation simulation grid.

The global ionisation evolution shows distinct patterns across different models (see Figure 3). While LOW-RES, MID-RES, and HIGH-RES simulations exhibit nearly identical reionisation histories due to shared parameter configurations ( $\zeta$  and  $T_{\text{vir}}(M_{\min})$ ), they differ substantially from both Faint and Bright Galaxies models. Specifically, the elevated  $T_{\text{vir}}(M_{\min})$  threshold in the LOW/MID/HIGH-RES ensemble postpones the onset of ionisation relative to the Faint Galaxies scenario, where smaller dark matter haloes facilitate earlier reionisation contributions. The Bright Galaxies model shows the most delayed ionisation, consequent to its high  $T_{\text{vir}}(M_{\min})$ . Furthermore, the augmented  $\zeta$  induces a contraction of the reionisation timescale ( $\Delta z_{\text{re}}$ ), resulting in intermediate  $\Delta z_{\text{re}}$  values for the LOW/MID/HIGH-RES simulations that bridge the extended Faint Galaxies and rapid Bright Galaxies regimes.

### 3.2 Models of foreground deflectors

We use the TNFW model (Navarro et al. 1997; Baltz et al. 2009) to describe the mass profiles of the foreground deflectors, which is adopted broadly to model dark matter haloes (Medezinski et al. 2016; Minor et al. 2017; Dai et al. 2018) that dominate galaxy clusters. The TNFW profile analytically renders the cluster lenses’ macro

mass distribution and realistically reflects their primary features, like concentration and virial mass. The 3D TNFW model can be given by (Baltz et al. 2009):

$$\rho(x) = \frac{\rho_s}{x(1+x)^2} \frac{r_t^2}{(xr_s)^2 + r_t^2}, \quad (11)$$

with  $x = \theta D_d / r_s$ , where  $\theta$  is the angular position of  $x$ .  $r_s$  and  $\rho_s$  are the scale radius and the characteristic density of the halo.  $r_s$  is calculated by  $r_{200} = r_s c$  and  $c$  is the concentration parameter, which is obtained via the mass-concentration relation (Child et al. 2018).  $r_t$  is the truncation radius, on account of the best-fit value of  $r_t$  in Oguri & Hamana (2011), we set  $r_t = 2.6r_{200}$ . The projected surface mass density of the TNFW model can be given by (Baltz et al. 2009):

$$\Sigma(x) = \frac{2r_s\rho_s\tau^2}{(\tau^2+1)^2} \left\{ \frac{\tau^2+1}{x^2-1} [1-F(x)] + 2F(x) - \frac{\pi}{\sqrt{\tau^2+x^2}} + \frac{\tau^2-1}{\tau\sqrt{\tau^2+x^2}} L(x) \right\}, \quad (12)$$

where

$$L(x) = \ln \left( \frac{x}{\sqrt{\tau^2+x^2} + \tau} \right), \quad (13)$$

and

$$F(x) = \frac{\cos^{-1}(1/x)}{\sqrt{x^2-1}}, \quad (14)$$

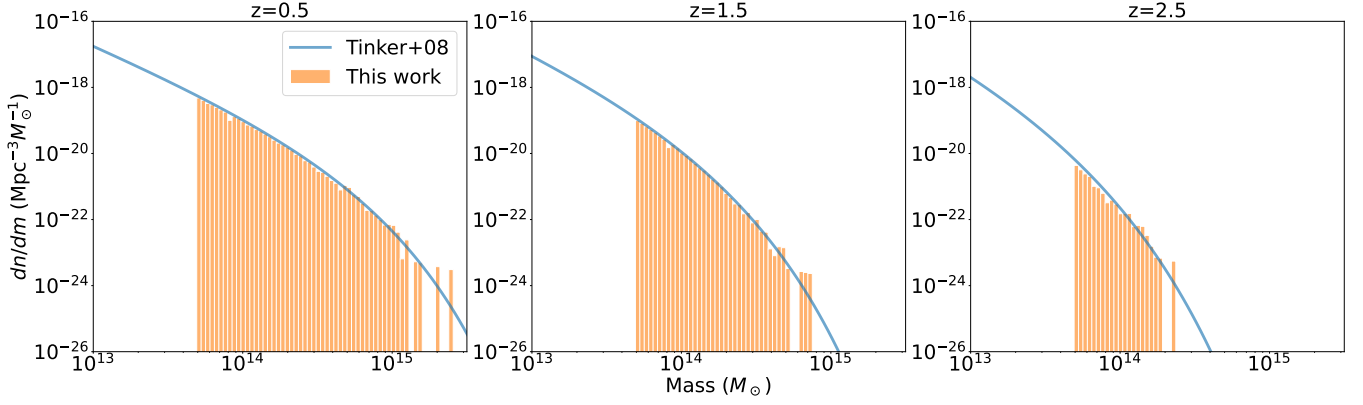


**Figure 4.** Comparison between the mass functions of the deflectors in our light cones (red points) and the theoretical outcomes given by Tinker et al. (2008) (blue lines) at redshifts  $z=0.5$ , 1.5, and 2.5, from left to right, respectively.

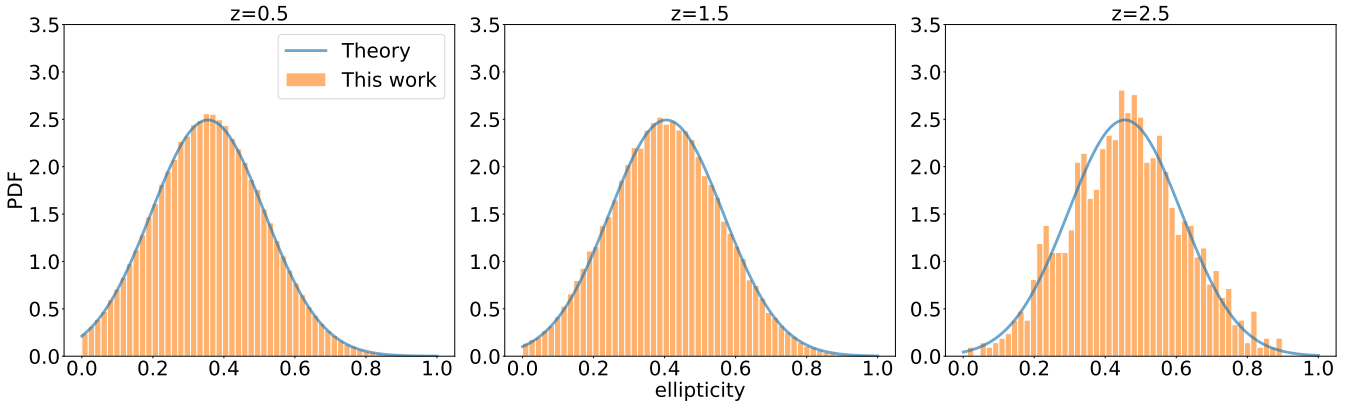


**Figure 5.** Comparison between the PDFs of projected mass ellipticity  $e$  of the deflectors in our light cone (orange bars) and theoretical outcomes of the mean  $e$  evolution given by Hopkins et al. (2005) with Gaussian dispersion  $\sigma_e = 0.16$  (blue lines) at redshifts  $z=0.5$ , 1.5, and 2.5, from left to right, respectively.

with  $\tau = r_t/r_s$ . Besides, the potential  $\psi$  can be expressed as (Baltz et al. 2009):

$$\begin{aligned} \psi(x) = & \frac{8\pi G \rho_s r_s^3}{c^2} \frac{1}{(\tau^2 + 1)^2} \left\{ 2\tau^2 \pi \left[ \tau - \sqrt{\tau^2 + x^2} + \tau \ln \left( \tau + \sqrt{\tau^2 + x^2} \right) \right] \right. \\ & + 2(\tau^2 - 1)\tau \sqrt{\tau^2 + x^2} L(x) + \tau^2(\tau^2 - 1) L^2(x) \\ & + 4\tau^2(x^2 - 1)F(x) + \tau^2(\tau^2 - 1) \left( \cos^{-1} \frac{1}{x} \right)^2 \\ & + \tau^2 [(\tau^2 - 1) \ln \tau - \tau^2 - 1] \ln x^2 \\ & \left. - \tau^2 [(\tau^2 - 1) \ln \tau \ln(4\tau) + 2 \ln(\tau/2) - 2\tau(\tau - \pi) \ln(2\tau)] \right\}. \end{aligned} \quad (15)$$

The deflection angle  $\alpha$  of the TNFW model can be derived from the gravitational potential  $\psi$  using Eq. (7). The elliptical case of the TNFW can be derived from the above spherical counterparts (Golse & Kneib 2002; Baltz et al. 2009). Therefore, each deflector in a given light cone can be characterized by six parameters: (R. A., Dec.) (angular position),  $\phi$  (position angle of the projected major axis),  $M_{200}$  (mass),  $z$  (redshift), and  $e$  (ellipticity, defined as  $e = 1 - q$ , where  $q$  is the axis ratio).

To build a light cone containing deflectors described by the TNFW

profile, one can randomly resample the above combination of six parameters according to the assumed distributions. Here, R. A. and Dec. are randomly generated with respect to uniform distributions. Regarding other parameters, the Python package HALOMOD (Murray et al. 2021) is used to provide the theoretical halo mass function at different redshifts, then  $M_{200}$  and  $z$  of deflectors are generated. For the halo mass function, we use the form given by Tinker et al. (2008):

$$\frac{dn}{dM} = f(\sigma) \frac{\bar{\rho}_m}{M} \frac{d \ln \sigma^{-1}}{dM}, \quad (16)$$

where  $\bar{\rho}_m = \Omega_m \rho_{\text{crit}}$ ,  $\Omega_m$  is the total matter density parameter, and the halo mass is defined as  $M_{200}$ . Specifically,  $M_{200} = \frac{800}{3} \rho_{\text{crit}} \pi r_{200}^3$ , with  $\rho_{\text{crit}}$  representing the critical density. The function  $f(\sigma)$  is parameterized as:

$$f(\sigma) = A \left[ \left( \frac{\sigma}{b} \right)^{-a} + 1 \right] e^{-c/\sigma^2}, \quad (17)$$

where the parameters  $a$ ,  $b$ ,  $c$ , and  $A$  are taken from Tinker et al. (2008),  $\sigma$  is the standard deviation of the linear density field smoothed on scale  $R$ :

$$\sigma^2 = \int P(k) \hat{W}(kR) k^2 dk. \quad (18)$$

Here,  $\hat{W}(kR)$  is the Fourier transform of the real-space top-hat filter

function of radius  $R$ .  $P(k)$  is the linear matter power spectrum as a function of wave number  $k$ , in HALOMOD, the fitting formula for the linear transfer function including baryons from Eisenstein & Hu (1998) is adopted. The low-mass threshold for the foreground deflectors is set to  $M_{200} = 5 \times 10^{13} M_{\odot}$ , and the maximum redshift cut for deflectors is set to  $z_{\max} = 4$ . Figure 4 presents the comparisons of the halo mass number density distributions extracted from our foreground light cones and the theoretical halo mass functions at redshifts  $z = 0.5, 1.5,$  and  $2.5$ , validating the resampling procedure. Besides, we draw the 2D projected ellipticity  $e$  of the mass distribution of haloes based on the formula in Hopkins et al. (2005): the redshift-dependent mean value of  $e$  evolves as  $\mu_e(z) = 0.33 + 0.05z$ , which is obtained from their large-volume, high-resolution  $\Lambda$ CDM  $N$ -body simulations. At  $z \simeq 0$ , the mean value of  $e$  is in high agreement with the observation of the mass distribution of local Abell clusters (Plionis et al. 1991), local  $e$  distribution is well described in Plionis et al. (1991) by a Gaussian distribution with dispersion  $\sigma_e = 0.16$ . Allgood et al. (2006) found that the 3D minor-to-major axis ratio of haloes up to  $M_{\text{vir}} = 2 \times 10^{14} M_{\odot}$  is well described by the Gaussian model with standard deviation  $\sim 0.1$  over the redshift range  $z = 0 \sim 3$ . Suto et al. (2016) showed no significant difference ( $\leq 15\%$ ) of standard deviation of 2D minor-to-major axis ratio of haloes with  $M_{\text{vir}} \gtrsim 6.25 \times 10^{13} M_{\odot}$  between  $z = 0 \sim 1$ . These results are also obtained based on  $N$ -body simulations. So we adopt  $\sigma_e = 0.16$  and fix it at all redshifts. The setting of  $\sigma_e$  can be improved based on more data in the future. Figure 5 shows the comparisons between the PDFs of the deflectors' ellipticities and the theoretical predictions at redshifts  $z = 0.5, 1.5,$  and  $2.5$ , validating our resampling procedure. At last, the projected position angles of deflectors  $\phi$  are sampled following a uniform distribution.

### 3.3 Lensing Simulation

With the light cone of deflectors constructed using the approach described in Sect. 3.2 and the source light cone built upon the ionisation simulations specified in Table 1, we performed multi-plane gravitational lensing simulations. This framework implements a ray-tracing algorithm that propagates light through the intervening matter distribution, generating lensed two-dimensional  $x_{\text{HI}}$  maps at different redshifts.

First, to mitigate the Poisson noise inherent in Monte Carlo sampling, we generated an ensemble of 50 independent light cones of deflectors, named as SET-FLC, and each light cone covers a  $2.5^{\circ} \times 2.5^{\circ}$  field of view. For comparative investigation, we adopt five source light cones: two of them are created on the EoR simulations with the assumptions of the EOS Faint Galaxies model and Bright Galaxies model separately, three of them are created on the HIGH/MID/LOW-RES simulations separately, see Sect. 3.1. For each of them, we perform 50 lensing simulations by connecting it to 50 light cones of deflectors from SET-FLC, and the final measurements of BSDs are the mean with  $1\sigma$  uncertainty of the outcomes of the MFP applied to all 50 realisations. Notably, the field of view of light cones of the HIGH/MID/LOW-RES simulations is one-sixteenth the size of the light cones in SET-FLC, measuring  $0.625^{\circ} \times 0.625^{\circ}$ . Hence, we equally divided each foreground light cone in SET-FLC into 16 subfields, each of which corresponds to one HIGH/MID/LOW-RES light cone for lensing simulations.

Second, we implement lensing simulations in the manner of the multi-lens-plane ray-tracing method using the Lenstronomy Python package (Birrer & Amara 2018; Birrer et al. 2021), and we place the haloes within the light cone onto a series of fixed lens planes at redshifts that are closest to them in terms of comoving distances.

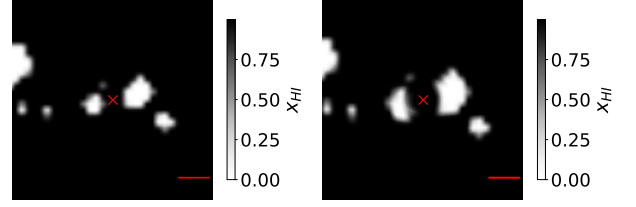


**Figure 6.** A showcase about how lensing changes the morphology of the ionised bubble of HIGH-RES at redshift  $z = 12$ . The panels from left to right are an unlensed  $x_{\text{HI}}$  map and the corresponding lensed one. The red segments at the bottom-right of each panel correspond to 50 arcsec, and the oblique cross symbols in the centre indicate the positions of foreground deflectors. This comparison shows that lensing significantly distorts the morphology of the ionised bubbles.

These lens planes span from  $z = 0.1$  up to  $z = 4$ , with a redshift spacing of  $\Delta z = 0.1$  for each lens plane. Typically, there are  $\sim 500$  haloes in a  $2.5^{\circ} \times 2.5^{\circ}$  light cone. The angular resolution of our lensing simulation is 5 arcsec, and the discussion for verifying this choice is presented in Sect. 5.3. Deflection angle maps in all lens planes are calculated using the Python package Lenstronomy (Birrer & Amara 2018; Birrer et al. 2021). On the  $i$ th lens plane, we also subtract the deflection angle caused by a constant mass sheet (denoted as  $\kappa_{\text{mean},i}$ ) equivalent to the average surface density of the plane, so that ray tracing is driven by density fluctuations.  $\kappa_{\text{mean},i}$  is the average convergence, uniformly sampled within the FOV range of the ray tracing map on the  $i$ th lens plane, and is expressed as:

$$\kappa_{\text{mean},i} \equiv \langle \kappa_i(\theta_i) \rangle_{\text{FOV}} \approx \frac{1}{N_{\text{pix}}} \sum_{p=1}^{N_{\text{pix}}} \kappa_i(\theta_p) \quad (19)$$

where  $N_{\text{pix}}$  is the number of pixels uniformly sampled,  $\kappa_i(\theta_i)$  is the convergence at angular position  $\theta_i$  on the  $i$ th lens plane, which is calculated by Eq. (9), and  $\theta_p$  is the angular position of a sampling point on the uniform grid. The sampling resolution is set to be the same as the resolution of the ray tracing map, which is 5 arcsec in the fiducial run. The deflection angle caused by the mass sheet of  $\kappa_{\text{mean},i}$  at angular position  $\theta$  is given by (Meneghetti 2022):

$$\alpha(\theta) = \kappa_{\text{mean},i}\theta. \quad (20)$$

The unlensed ionisation maps are created using the same approach and configurations mentioned above, but no deflection angles are included. Therefore, the unlensed ionisation maps are essentially an upsampling of the primordial 2D  $x_{\text{HI}}$ , which maintains consistent resolution, theoretical and numerical assumptions when measuring the difference between lensed and unlensed BSDs.

## 4 ESTIMATION OF BSD

The results of the lensing simulation show that gravitational lensing alters the morphology of ionised bubbles. For example, as shown in Figure 6, the shapes of the two ionised bubbles in the central region are distorted by foreground lensing. This distortion extends beyond mere visual changes; it also impacts the statistical properties of ionised bubbles, such as the BSD. To characterise this lensing-induced modification, we require a robust BSD quantification methodology. The present section details our approach for accurate BSD measurement.

We apply the MFP method (Mesinger & Furlanetto 2007) to measure the BSD from the 2D unlensed  $x_{\text{HI}}$  map and the lensed  $x_{\text{HI}}$  map.

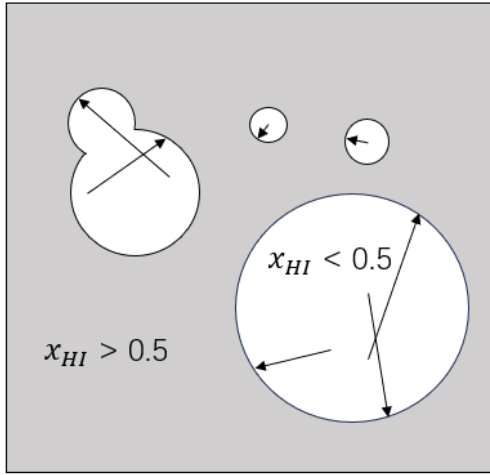


**Figure 7.** A schematic diagram of using the MFP method to measure the BSD. This picture is a cartoon diagram of a two-dimensional  $x_{\text{HI}}$  map during EoR, we randomly select starting points in ionised regions of this map where  $x_{\text{HI}} < 0.5$  (white regions) and shoot rays in random directions until the rays hit the edge of the un-ionised region (dark-coloured region,  $x_{\text{HI}} > 0.5$ ) or the boundaries of map. The length of the ray’s path is used to characterise the size of the ionised region. By repeating this process, we can obtain the probability distribution of ionised regions’ size across the entire  $x_{\text{HI}}$  map.

We note that the BSD referred to in this paper is apparent BSD. By comparing the BSD before and after lensing, we were able to quantify the impact of lensing on the BSD. The MFP method is one of the most accurate approaches for BSD measurements compared to other methods in the literature, as demonstrated in [Lin et al. \(2016\)](#), it performs exceptionally well in recovering the intrinsic BSD. This method is based on a Monte Carlo algorithm. We randomly select points within the ionised regions on the two-dimensional  $x_{\text{HI}}$  map and shoot rays in random directions. The rays stop when they encounter the boundary of the un-ionised region, which is defined as the area where the ionisation fraction is less than 0.5, or stop when they encounter the boundary of the map. The length of the path travelled by the ray is used to characterise the size of the ionised region (as shown in Figure 7). Continuously repeating this process allows us to determine the probability distribution of ionised bubble size. In this work, we use the Python package `Tools21cm` ([Giri et al. 2020](#)) to perform the MFP method to generate BSD for each ionisation model. For  $z_s = 12$  and 14, the operation of randomly shooting rays is repeated  $10^6$  times. At  $z_s = 9$ , the ionised region is much larger than that of  $z_s = 12$  and 14, we set the number of randomly shooting rays to be  $10^8$ , and we discuss the influence of the iteration number in Sect. 5.4. Furthermore, the thickness of the 2D slices used to measure the BSD in MFP method is uniformly set to 2 cMpc. In this process, we generate the slices with a thickness of 2 cMpc using linear interpolation; such a slice incorporates information from multiple original ionisation simulation slices. Besides, to obtain robust results, we averaged the BSD measurements over the 50 lensing simulation realisations.

## 5 RESULTS

This section presents the lensing effects on the BSD during EoR and the influence of simulation setups on the lensing effects on BSD, such as the construction of the source light cone (Sect. 5.2), the

construction of lens light cone and ray-tracing simulation (Sect. 5.3), and the MFP algorithm used to extract the BSDs (Sect. 5.4).

### 5.1 Lensing Effects on BSD

Gravitational lensing induces significant distortions in the BSD in the large bubble regime, particularly during the early stage of the EoR ( $x_{\text{HI}} \lesssim 0.05$ ). These distortions manifest as an enhancement in the expected abundance of large bubbles across all source ionisation models, persisting over an extended timescale corresponding to a redshift interval of  $\Delta z \gtrsim 2$  (see Figure 8). Specifically, for the EOS Faint Galaxies model, we observe a 219% increase in the abundance of bubbles with bubble size  $R > 15$  cMpc at redshift  $z_s = 14$ , while the EOS Bright Galaxies model shows a more pronounced enhancement of 832%.

Besides, the effects of lensing on BSD evolve along redshifts, e.g., results from HIGH-RES simulations demonstrate that at  $z_s = 14$  with  $Rdp/dR = 10^{-6}$ , the bubble sizes increase by approximately 15%, while at  $z_s = 12$ , the increase remains significant at 8%. However, as reionisation progresses, the larger size of the ionised bubbles compared to the lensing cross-section of galaxy clusters in the later stage of EoR makes their properties less sensitive to distortion, such as the lensing effects on BSDs are suppressed at  $z_s = 9$  (see Figure 8).

For small-scale bubbles, the BSDs remain unaffected by lensing throughout the entire EoR across all ionisation simulations down to 2 cMpc. This defines the nominal lower bound of the BSD measurement, and the lensing effect on bubbles below it remains mysterious. It will be discussed in Sect. 5.4 and will be investigated in detail in the future.

### 5.2 Influence of Source Models on the Estimation of BSD

BSDs are intrinsically sensitive to ionisation parameters, which might lead to various influences of lensing on BSDs. For example, the ionisation parameters minimum halo mass which host ionising sources  $M_{\text{min}}$  and ionising efficiency  $\zeta$ , where, increasing  $M_{\text{min}}$  shifts the BSD toward larger bubbles, whereas a larger  $\zeta$  accelerates the growth of ionised bubbles ([Mesinger et al. 2016](#)). Expressly, at  $z_s = 9$ , compared to the BSD of the EOS Faint Galaxies model, the BSD of EOS Bright Galaxies model exhibits more pronounced large ionised bubbles distribution for its greater  $M_{\text{min}}$  as shown in the bottom-left panel in Figure 8, which aligns with the difference between the simulation results of bright galaxies-dominated model and the faint galaxies-dominated model in [Lu et al. \(2024\)](#).

Besides, the Poisson uncertainty may affect the robustness of the measurements of lensing effects on BSDs, which is initially tied to the abundance of the corresponding dark matter haloes ([Mesinger et al. 2011](#)). Poisson uncertainty on the lensing effects on BSDs evolves with the reionisation stage and the bubble scale. For example, when it comes to large bubbles ( $R \gtrsim 10$  cMpc) at  $z = 12$ , the difference between intrinsic BSDs of HIGH/MID/LOW-RES source models (Figure 8) is largely due to the significant fractional Poisson uncertainty caused by the rarity of bubbles. To better quantify the lensing effects on BSDs, the impacts of Poisson uncertainty need to be improved by employing large-scale simulations with sufficient statistics in future studies.

Moreover, [Mesinger & Furlanetto \(2007\)](#) showed that a box size of 100 cMpc would underestimate the size of bubbles larger than the characteristic bubble size at  $z_s = 9$ . Along with the progress of reionisation, more large bubbles are ‘missed’ due to the limited box

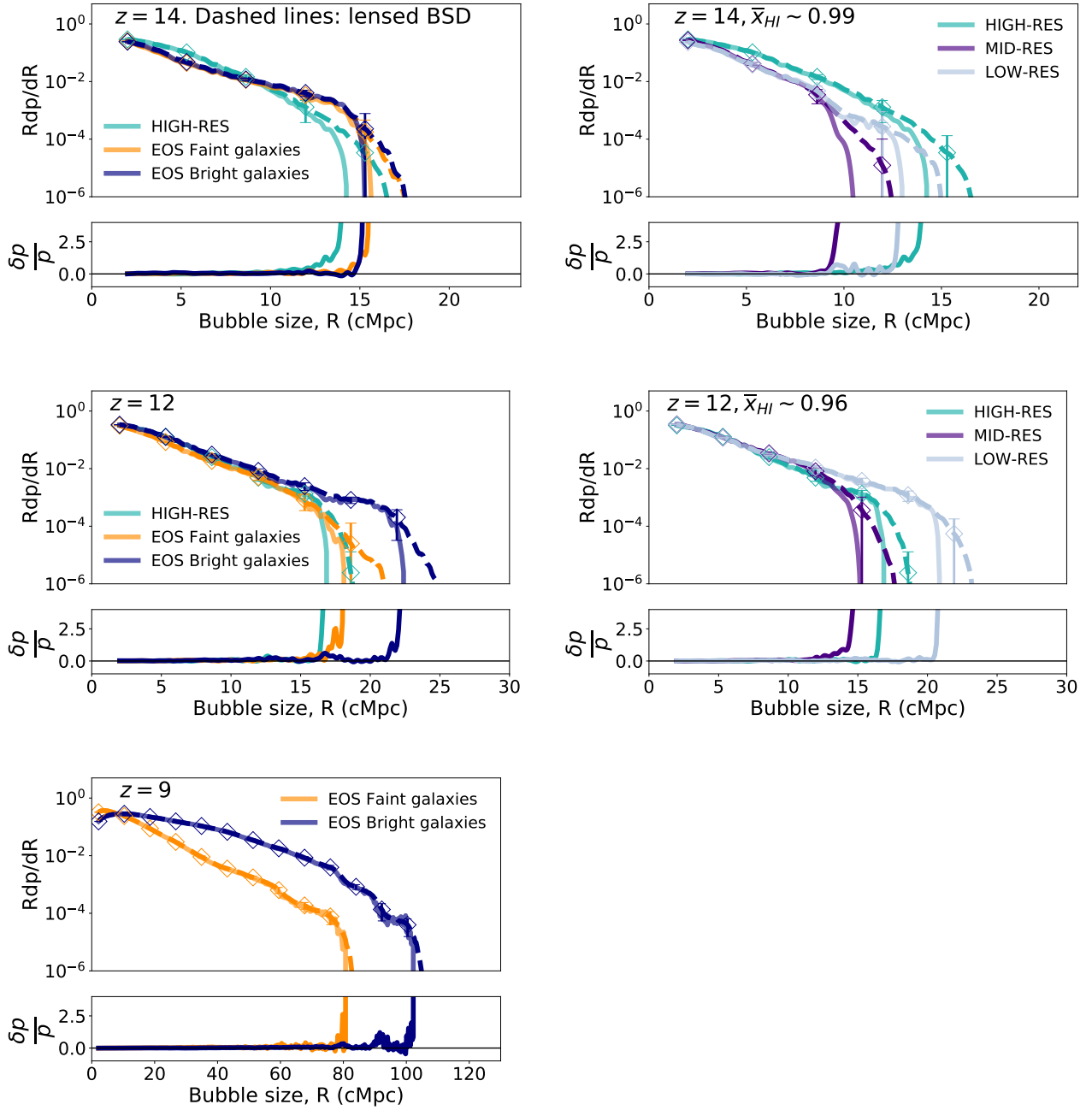


**Figure 8.** Bubble Size Distribution (BSD) for lensed and unlensed cases at redshifts  $z = 14$ ,  $z = 12$ , and  $z = 9$ , from top to bottom. Solid lines indicate unlensed BSD and dashed lines represent lensed BSD. Different colours represent the results of different ionisation models. The left panels of  $z = 12$  and  $z = 14$  compare the results of three different ionisation models which have different ionisation parameter settings ( $\zeta$  and  $T_{\text{vir}}(M_{\text{min}})$ ), while the right panels compare results of three simulations with the same ionisation parameters but different ionisation simulation resolutions. The error bars on the lensed curves correspond to  $1\sigma$  uncertainties in the 50 lens light cone results. At the small  $R$  end, the error bars are hardly visible because the uncertainties are small. Below each chart, we show the relative difference between the lensed and unlensed BSD, given by  $\delta p/p = (\text{PDF}' - \text{PDF})/\text{PDF}$  where  $\text{PDF}'$  is the bubble size probability distribution function under the lensed situation, and  $\text{PDF}$  is that of the unlensed situation. Besides, the slice thickness used for BSD measuring for each model is fixed to 2 cMpc here.

size. Hence, the larger the ionised fraction, the larger the reionisation simulation box required to capture the ionisation topology (see Figure 7 and Figure 10 in Mesinger & Furlanetto (2007)). At redshifts above 12, the ionisation fraction is less than 0.05, and bubble sizes are approximately 0 to 25 cMpc, which is far smaller than the

box size of source simulations ( $\lesssim 0.06 \times$  the size of EOS simulation and  $\lesssim 0.2 \times$  the size of HIGH/MID/LOW-RES simulations<sup>6</sup>).

<sup>6</sup> For the HIGH-RES, MID-RES, and LOW-RES simulations, the light cone extends approximately 100 to 125 cMpc perpendicular to the line of sight at

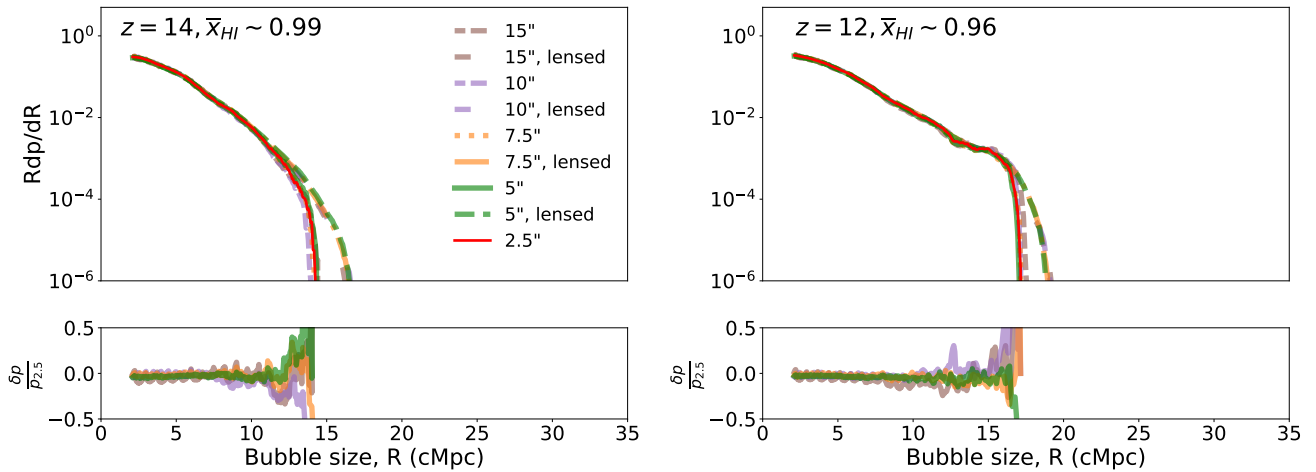


**Figure 9.** The influence of ray-tracing resolution on BSD. These panels show lensed and unlensed BSD of HIGH-RES when ray-tracing resolution is set to 5, 7.5, 10, and 15 arcsec at redshifts 12 and 14, respectively. We also show the unlensed BSD when the resolution is 2.5 arcsec as the red solid lines. BSD is measured by the MFP method (Mesinger & Furlanetto 2007). The lower panel shows the unlensed BSD difference compared to the case of 2.5 arcsec, given by  $\delta p / p_{2.5} = (\text{PDF}^* - p_{2.5}) / p_{2.5}$ . Where  $\text{PDF}^*$  is the bubble size probability distribution function under different lensing simulation resolutions, and  $p_{2.5}$  refers to the bubble size probability distribution of the case of 2.5 arcsec.

However, at redshift 9, with a larger ionisation fraction of about 0.2 and bubble sizes reaching 60 to 80 cMpc, the limited box size could impact BSD measurements in HIGH/MID/LOW-RES. In the latter half stages of reionisation ( $x_{\text{HI}} < 0.5$ ), the size of large ionised bubbles exceeds 125 cMpc (Lu et al. 2024), causing the limited scales of HIGH/MID/LOW-RES simulations to have no chance in capturing the information of maximum bubble sizes. In this work, we only retain BSD results when the simulation box size is at least five times larger than the size of the largest bubble size, which relieves the effect of a finite box volume in ionised bubble size estimation. Large-scale simulations can address this limitation as well.

In addition, across all models and parameter choices tested, lensing by galaxy clusters affects the BSD in the large-size region because of its significant cutoff, which is a physical effect rather than a numerical assumption. For instance, the ionisation-field generation in 21cmFAST is based on an excursion-set algorithm within the extended Press–Schechter formalism (Furlanetto et al. 2004); this semi-numeric approach reproduces key properties of ionised regions, such as their topology and power spectra, in good agreement with radiative-transfer simulations (Mesinger & Furlanetto 2007; Lin et al. 2016), and has therefore been widely adopted. The excursion-set formalism predicts an exponential cutoff in the BSD at the large size end (Furlanetto et al. 2004). The correlation between the cutoff positions and combinations of reionisation parameters suggests that information about the BSD cutoff provides a useful handle for constraining reionisation physics. Hence, using 21cmFAST, we reran reionisation simulations with identical simulation seeds to test how this cutoff depends on  $M_{\text{min}}$  and  $\zeta$ , finding at  $z = 12$  and  $z = 14$  that decreasing  $M_{\text{min}}$  tends to shift the cutoff to larger  $R$ , plausibly because a lower threshold increases the abundance of ionising sources, triggering earlier reionisation and facilitating more frequent and efficient mergers of ionised regions. We also find that increasing  $\zeta$  tends to move the cutoff to larger  $R$ , as expected from the enhanced

ionising-photon budget. Tests based on three independent comparison experiments with different random seeds all support the above results, demonstrating a clear dependence of the cutoff scale on the reionisation parameters. Owing to the limited simulation volume and the vast parameter space, we restrict ourselves here to a set of simple tests and exploratory analyses; a statistically comprehensive quantification of how reionisation parameters and lensing jointly impact the BSD cutoff will be investigated in future work.

### 5.3 Influence of the Setups of Lensing Simulations on the Estimation of BSD

Assumptions adopted in lensing simulation might introduce uncertainties and bias, which can not be ignored. First, we assume a uniform spatial distribution of the deflectors, neglecting the clustering of haloes and filamentary structures on cosmic scales. Second, our deflector mass profile is a single primary halo per deflector, while observational evidence suggests that accurate mass reconstructions of a galaxy cluster sometimes require multiple subhaloes, additional primary haloes, or external shear (Keeton 2001; Richard et al. 2007; Caminha et al. 2016; Sharon et al. 2020a). As the presence of line-of-sight haloes can increase the probability of lensing events (Li et al. 2019), the effect of ignoring extra haloes along the line of sight leads to an underestimation of the abundance of lensing events, thereby underestimating the impact of lensing on the BSD. Moreover, apart from the TNFW model, the mass profile of galaxy clusters can also be described by other lens models (such as the Pseudo Isothermal Elliptical Mass Distribution model (Kassiola & Kovner 1993; Árdís Elíasdóttir et al. 2007; Sharon et al. 2020b)), which gives various outcomes potentially. Above all, our assumptions lead to a lower limit of lensing effects on the BSDs. To better quantify the lensing effects on BSDs, we may model lensing light cones with cosmological simulations to involve (i) more realistic spatial distributions of deflectors, and (ii) more comprehensive mass maps of deflectors.

Furthermore, numerical setups for the lensing simulation may also raise uncertainties and bias, such as insufficient ray-tracing resolution in lensing simulations, which smooths small-scale structures of

different redshifts, while for the EOS simulations, it is approximately 400 to 500 cMpc.

lenses and sources, influencing the robustness of the results. To avoid this issue, we examine resolution dependence by testing values of 5, 7.5, 10, and 15 arcsec for the HIGH-RES model, measuring both lensed and unlensed BSDs at redshifts  $z_s = 12$  and 14 (Figure 9). For convergence testing, we include an additional high-resolution case (resolution = 2.5 arcsec, shown as the red solid lines for unlensed BSD in Figure 9). The results reveal diminishing differences in BSD values with decreasing resolution, with close agreement between the outcomes in the cases with angular resolutions of 2.5 and 5 arcsec. The relative difference of these two cases is  $< 10\%$  except for the largest size end. Therefore, we use 5 arcsec as the angular resolution in our lensing simulation.

#### 5.4 Influence of the Setups of MFP on the Estimation of BSD

The resolution of lensing and EoR simulations determines the lower limits of the BSD measurement with MFP, i.e., the parameter of the shortest travel distance of testing particles in MFP should be larger than the coarsest pixel size adopted in the above simulations because it reveals no physical information when travel distances of testing particles are smaller than pixel sizes (Mesinger et al. 2011). Specifically, if we set the shortest travel distance to be 0.5 cMpc at  $z_s = 14$  (HIGH-RES EoR simulation), approximately 40% of the shortest travel distances of random testing particles in the MFP algorithm are less than this; in the EOS Bright Galaxies model, this fraction increases to about 65%, where the corresponding resolution is about 1.56 cMpc. When we measure BSDs of lensed EoR maps with the resolution of lensing simulations, the corresponding resolution is about 0.25 cMpc at  $z_s = 14$ . Conservatively, we choose 2 cMpc as the shortest travel distances in MFP, which is much smaller than the typical sizes of the largest bubbles (15 ~ 25 cMpc at  $z_s = 12$  and 10 ~ 20 cMpc at  $z_s = 14$ ). This setup does not affect our conclusion that lensing significantly affects the largest bubbles. However, to accurately investigate the lensing effects on small bubbles, we have to employ simulations of lensing and EoR with the required resolutions.

Besides, the measurement of BSDs via the MFP method involves intrinsic Monte Carlo sampling uncertainties, which means that the iteration count  $i$  should be large enough to eliminate the influence due to shot noise. We conducted a test comparing BSD measurements across different iteration numbers to quantify potential numerical noise due to finite sampling. At  $z_s > 12$  and  $z_s = 9$ , our baseline uses  $i = 10^6$  and  $i = 10^8$  Monte Carlo iterations, respectively; for validation we increase to  $i = 10^8$  (for  $z_s > 12$ ) and  $i = 10^9$  (for  $z_s = 9$ ). At the latter stage of EoR, the size of the ionised region is large and a higher iteration count  $i$  is needed. We apply these tests to the HIGH-RES runs at  $z_s = 12$  and 14, and to the EOS Bright and Faint galaxies models at  $z_s = 9$ . We test both lensed and unlensed BSD. For  $z_s = 12$  and 14, we recompute the lensed BSD for all 50 lens cones with  $i = 10^8$  (i. e., we totally reproduce the final result of HIGH-RES shown in Figure 8 using  $i = 10^8$ ). At  $z_s = 9$ , the  $i = 10^9$  test is only performed for randomly 5 of the 50 cones (i. e., 10%) due to the large calculation resource requirement of the setting of  $i = 10^9$ . Figure 10 and Figure 11 show that the BSDs measured in the standard case and the validation case are very close, especially at  $z_s = 12$  and 14. Relative difference is  $< 10\%$  except for the largest size end. Confirming that our choice of the number of iterations is reliable at these redshifts.

## 6 CONCLUSIONS

In this study, we conducted a suite of lensing ray-tracing simulations in the case of the multi-lens-plane with various ionisation models to investigate the impacts of lensing by galaxy clusters on ionisation structures during the EoR. By comparing the BSD of lensed and unlensed 2D  $x_{\text{HI}}$  maps using the MFP method, we found that gravitational lensing significantly increases the number of bubbles at the large size end due to the lensing magnification. In contrast, the statistics of small-scale bubbles remain unaffected by lensing down to the bubble size of 2 cMpc throughout the entire EoR. Besides, different ionisation models yield varying results. Specifically, in the ionisation model dominated by the EOS Faint Galaxies model, the number of bubbles larger than 15 cMpc increases by 219% at a redshift of 14. Conversely, in the model dominated by the EOS Bright Galaxies model, this number increases by 832%.

In addition, the lensing effects on BSD change with redshift, as the influence of lensing magnification is sensitive to the topology of the ionisation bubbles. For instance, according to the redshift ranges defined in Jamieson et al. (2024) which traces the ionised bubble merging path using data products from the THESAN simulations (Kannan et al. 2022) as sources, the evolution of ionised bubbles in a faint galaxies dominated reionisation model can be divided into three distinct stages: (i) Initial Expansion Phase ( $z \gtrsim 11$ ); (ii) Merging Phase ( $z \approx 9-11$ ); (iii) Rapid Expansion Phase ( $z \lesssim 9$ ). For the case of the faint galaxy dominated models as sources in our lensing simulations, we found that the lensing effects on BSD significantly exist in the bubble Initial Expansion Phase and are suppressed in the Merging Phase and Rapid Expansion Phase, as illustrated in Figure 8 in Sect. 5.

To verify the reliability of our conclusions, we examined how various simulation settings influence the outcomes. We quantified the lensing effects on the BSD using five ionisation simulations that varied in the minimum ionising source mass, ionisation efficiency, or ionisation simulation resolution (as illustrated in Sect. 3.1). The results across these simulations consistently demonstrated that lensing significantly impacts the BSD during the early stages of the EoR, specifically by increasing the expected number of large-scale bubbles. Moreover, we assessed the influence of different lensing simulation ray-tracing resolutions and iteration numbers in the MFP method used for BSD measurement, confirming the tendency of our findings, which are shown in Sect. 5.3 and Sect. 5.4. However, the pixelization of the mock source planes might underestimate the lensing effects on small-scale ionisation bubbles, which can be enhanced with future finer ionisation simulations. The box size of the mock might lead to statistical effects in the size distribution of large bubbles, as simultaneously achieving both high angular resolution and a large box size remains a challenge.

Notably, we adopt relatively simple assumptions regarding the lens and source populations to illustrate the tendency of the lensing effects on BSD by galaxy clusters. For instance, the source models contain different ionisation parameters, such as  $M_{\text{min}}$  and  $\zeta$ , leading to various lensing effects at given redshifts. Besides, the angular positions of the deflectors in our simulations are generated via the Monte Carlo method based on the assumption of uniform distribution without accounting for large-scale structures like cosmic filaments, which can be improved by employing haloes or even particles from N-body simulations directly. The mass distribution of the deflectors adheres to the TNFW model but does not include contributions from subhaloes, which can be addressed using Semi-analytic models or hydrodynamic simulations. Last but not least, while we present a theoretical exploration of lensing effects on BSD, it is critical to

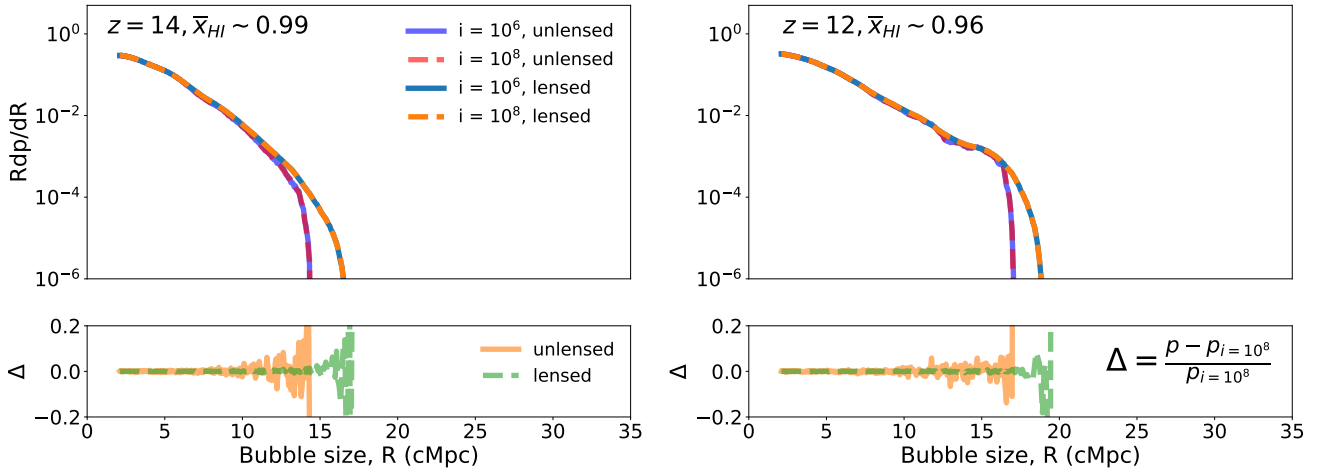


**Figure 10.** Robustness test of iteration counts in the MFP method for BSD measurement at  $z_s = 14$  and  $z_s = 12$  for HIGH-RES model. The upper panels present the standard implementation with  $i = 10^6$  iterations in the MFP algorithm (solid curves) and the realisation with  $i = 10^8$  iterations (dashed curves) for comparison. The lower panels show the relative BSD difference between realisations with  $i = 10^6$  and  $i = 10^8$ , respectively. Left and right panels demonstrate the comparison when the source planes are located at  $z_s = 14$  and  $z_s = 12$ , respectively.

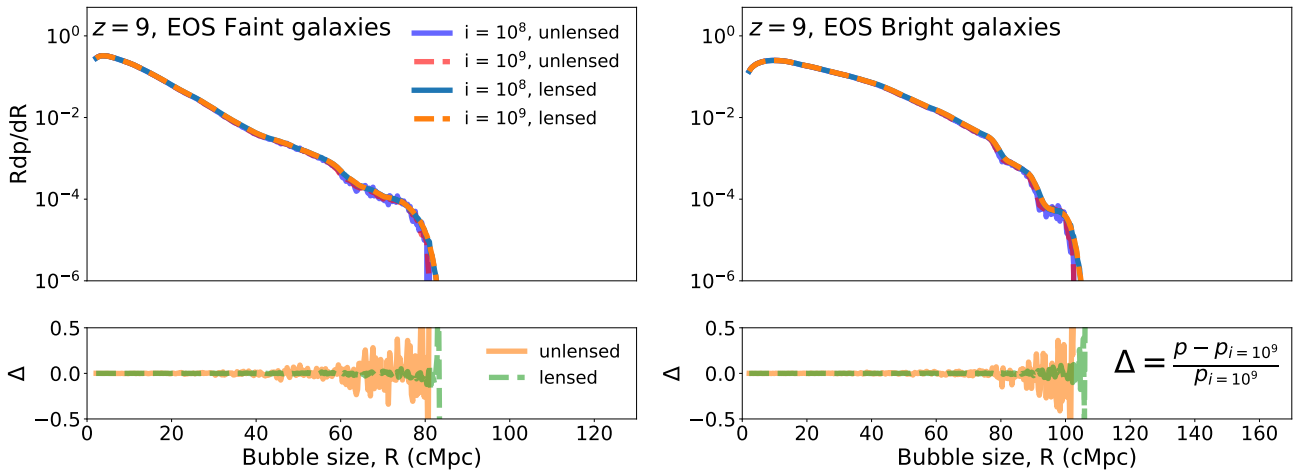


**Figure 11.** Robustness test of iteration counts in the MFP method for BSD measurement at  $z_s = 9$  for the EOS Bright galaxies and Faint galaxies model. The upper panels present the standard implementation with  $i = 10^8$  iterations in the MFP algorithm (solid curves) and the realisation with  $i = 10^9$  iterations (dashed curves) for comparison. The lower panels show the relative BSD difference between realisations with  $i = 10^8$  and  $i = 10^9$ , respectively. Left and right panels demonstrate the situation of EOS Bright galaxies and Faint galaxies model, respectively.

consider instrumental effects if one intends to constrain the statistics of sources and lenses with the lensing effects on BSD.

In summary, gravitational lensing caused by galaxy clusters leads to a non-negligible influence on the statistical properties of the ionisation structures during EoR, such as the size distribution of ionisation bubbles. The emergence of next-generation radio telescopes, such as the SKA, offering sufficient sensitivity and extensive sky coverage, will enable the observation of ionisation bubble statistics during the EoR as expected, which will promote astrophysical and cosmological investigations. Therefore, it is essential to carefully consider the lensing effects in relevant studies to ensure accurate and unbiased interpretations of observations.

## ACKNOWLEDGEMENTS

This work is supported by the Ministry of Science and Technology of China (grant Nos. 2020SKA0110100). We thank Bin Liu and Yidong Xu for insightful discussions. N.L. acknowledges the support of the science research grants from the China Manned Space Project (No. CMS-CSST-2021-A01) and the CAS Project for Young Scientists in Basic Research (No. YSBR-062). HYS acknowledges the support from NSFC of China under grant 12533008, Key Research Program of Frontier Sciences, CAS, Grant No. ZDBS-LY-7013 and Program of Shanghai Academic/Technology Research Leader. Z.Z. acknowledges the support from the National Science Foundation of China (Grant No. 12203085). We thank ChatGPT for polishing the English in this paper.

## DATA AVAILABILITY

The data utilized in this study will be provided upon reasonable request.

## REFERENCES

- Abdurashidova Z., et al., 2022, *ApJ*, **925**, 221
- Allgood B., Flores R. A., Primack J. R., Kravtsov A. V., Wechsler R. H., Faltenbacher A., Bullock J. S., 2006, *MNRAS*, **367**, 1781
- Baltz E. A., Marshall P., Oguri M., 2009, *J. Cosmology Astropart. Phys.*, **2009**, 015
- Barkana R., Loeb A., 2001, *Phys. Rep.*, **349**, 125
- Barry N., et al., 2019, *ApJ*, **884**, 1
- Bartelmann M., 2010, *Classical and Quantum Gravity*, **27**, 233001
- Birrer S., Amara A., 2018, *Physics of the Dark Universe*, **22**, 189
- Birrer S., et al., 2021, *The Journal of Open Source Software*, **6**, 3283
- Blain A. W., 1996, *MNRAS*, **283**, 1340
- Borgeest U., von Linde J., Refsdal S., 1991, *A&A*, **251**, L35
- Caminha G. B., et al., 2016, *A&A*, **587**, A80
- Castellano M., et al., 2016, *The Astrophysical Journal Letters*, **818**, L3
- Castellano M., et al., 2018, *The Astrophysical Journal Letters*, **863**, L3
- Castellano M., Menci N., Romanello M., 2023, Constraints On Dark Matter From Reionization ([arXiv:2301.03854](https://arxiv.org/abs/2301.03854)), <https://arxiv.org/abs/2301.03854>
- Child H. L., Habib S., Heitmann K., Frontiere N., Finkel H., Pope A., Morozov V., 2018, *ApJ*, **859**, 55
- Ciardi B., Ferrara A., 2005, *Space Sci. Rev.*, **116**, 625
- Dai L., Venumadhav T., Kurov A. A., Miralda-Escud J., 2018, *The Astrophysical Journal*, **867**, 24
- Datta K. K., Bharadwaj S., Choudhury T. R., 2007, *Monthly Notices of the Royal Astronomical Society*, **382**, 809–818
- Dayal P., 2019, *Proceedings of the International Astronomical Union*, **15**, 43–43
- Dayal P., Giri S. K., 2024, *MNRAS*, **528**, 2784
- DeBoer D. R., et al., 2017, *Publications of the Astronomical Society of the Pacific*, **129**, 045001
- Dijkstra M., 2014, *Publ. Astron. Soc. Australia*, **31**, e040
- Doussot A., Semelin B., 2022, *A&A*, **667**, A118
- Eisenstein D. J., Hu W., 1998, *ApJ*, **496**, 605
- Endsley R., Stark D. P., 2022, *Monthly Notices of the Royal Astronomical Society*, **511**, 6042–6054
- Er X., Li G., Mao S., Cao L., 2013, *MNRAS*, **430**, 1423
- Finkelstein S. L., et al., 2019, *ApJ*, **879**, 36
- Furlanetto S. R., Oh S. P., 2016, *MNRAS*, **457**, 1813
- Furlanetto S. R., Zaldarriaga M., Hernquist L., 2004, *ApJ*, **613**, 1
- Furlanetto S. R., Oh S. P., Briggs F. H., 2006, *Phys. Rep.*, **433**, 181
- Giri S. K., Mellema G., Dixon K. L., Iliev I. T., 2018, *MNRAS*, **473**, 2949
- Giri S., Mellema G., Jensen H., 2020, *The Journal of Open Source Software*, **5**, 2363
- Golse G., Kneib J. P., 2002, *A&A*, **390**, 821
- Greig B., Mesinger A., 2015, *MNRAS*, **449**, 4246
- Hopkins P. F., Bahcall N. A., Bode P., 2005, *ApJ*, **618**, 1
- Iliev I. T., Mellema G., Pen U. L., Merz H., Shapiro P. R., Alvarez M. A., 2006, *MNRAS*, **369**, 1625
- Jamieson N., et al., 2024, *arXiv e-prints*, p. [arXiv:2411.08943](https://arxiv.org/abs/2411.08943)
- Jones E., Smith B., Davé R., Narayanan D., Li Q., 2024, *MNRAS*, **535**, 1293
- Kannan R., Garaldi E., Smith A., Pakmor R., Springel V., Vogelsberger M., Hernquist L., 2022, *MNRAS*, **511**, 0008
- Kassiola A., Kovner I., 1993, *ApJ*, **417**, 450
- Katz H., Kimm T., Ellis R. S., Devriendt J., Slyz A., 2023, *MNRAS*, **524**, 351
- Keeton C. R., 2001, Computational Methods for Gravitational Lensing ([arXiv:astro-ph/0102340](https://arxiv.org/abs/astro-ph/0102340)), <https://arxiv.org/abs/astro-ph/0102340>
- Kolopanis M., et al., 2019, *ApJ*, **883**, 133
- Larson R. L., et al., 2022, *The Astrophysical Journal*, **930**, 104
- Li N., et al., 2019, *ApJ*, **878**, 122
- Lima M., Jain B., Devlin M., Aguirre J., 2010, *ApJ*, **717**, L31
- Lin Y., Oh S. P., Furlanetto S. R., Sutter P. M., 2016, *MNRAS*, **461**, 3361
- Liu A., Shaw J. R., 2020, *PASP*, **132**, 062001
- Lu T.-Y., Mason C. A., Hutter A., Mesinger A., Qin Y., Stark D. P., Endsley R., 2024, *MNRAS*, **528**, 4872
- Malhotra S., Rhoads J. E., 2006, *ApJ*, **647**, L95
- Mao Y., Tegmark M., McQuinn M., Zaldarriaga M., Zahn O., 2008, *Phys. Rev. D*, **78**, 023529
- Mason C. A., et al., 2015, *ApJ*, **805**, 79
- Mason C. A., Treu T., Dijkstra M., Mesinger A., Trenti M., Pentericci L., de Barros S., Vanzella E., 2018, *ApJ*, **856**, 2
- McQuinn M., Zahn O., Zaldarriaga M., Hernquist L., Furlanetto S. R., 2006, *ApJ*, **653**, 815
- McQuinn M., Lidz A., Zahn O., Dutta S., Hernquist L., Zaldarriaga M., 2007, *MNRAS*, **377**, 1043
- Medezinski E., Umetsu K., Okabe N., Nonino M., Molnar S., Massey R., Dupke R., Merten J., 2016, *ApJ*, **817**, 24
- Mellema G., Koopmans L., Shukla H., Datta K. K., Mesinger A., Majumdar S., 2015, in *Advancing Astrophysics with the Square Kilometre Array (AASKA14)*. p. 10 ([arXiv:1501.04203](https://arxiv.org/abs/1501.04203)), [doi:10.22323/1.215.0010](https://arxiv.org/abs/1501.04203)
- Meneghetti M., 2022, Introduction to Gravitational Lensing: With Python Examples
- Mertens F. G., et al., 2020, *MNRAS*, **493**, 1662
- Mesinger A., Furlanetto S., 2007, *ApJ*, **669**, 663
- Mesinger A., Furlanetto S., Cen R., 2011, *MNRAS*, **411**, 955
- Mesinger A., Greig B., Sobacchi E., 2016, *MNRAS*, **459**, 2342
- Minor Q. E., Kaplinghat M., Li N., 2017, *ApJ*, **845**, 118
- Mishra A., Murmu C. S., Datta K. K., Choudhuri S., Majumdar S., Nasreen I., Ali S. S., 2024, Detecting ionized bubbles around luminous sources during the reionization era using HI 21-cm signal ([arXiv:2408.01681](https://arxiv.org/abs/2408.01681)), <https://arxiv.org/abs/2408.01681>
- Morales M. F., Wyithe J. S. B., 2010, *ARA&A*, **48**, 127
- Murray S. G., Greig B., Mesinger A., Muñoz J. B., Qin Y., Park J., Watkinson C. A., 2020, *Journal of Open Source Software*, **5**, 2582
- Murray S. G., Diemer B., Chen Z., Neuhold A. G., Schnapp M. A., Peruzzi T., Blevins D., Engelman T., 2021, *Astronomy and Computing*, **36**, 100487
- Naidu R. P., Tacchella S., Mason C. A., Bose S., Oesch P. A., Conroy C., 2020, *ApJ*, **892**, 109
- Naoz S., Barkana R., 2008, *MNRAS*, **385**, L63
- Narayan R., Bartelmann M., 1996, *arXiv e-prints*, pp astro-ph/9606001
- Navarro J. F., Frenk C. S., White S. D. M., 1997, *ApJ*, **490**, 493
- Oguri M., Hamana T., 2011, *Monthly Notices of the Royal Astronomical Society*, **414**, 1851
- Parsons A. R., et al., 2010, *The Astronomical Journal*, **139**, 1468
- Planck Collaboration et al., 2016, *A&A*, **594**, A13
- Planck Collaboration et al., 2020, *A&A*, **641**, A6
- Plionis M., Barrow J. D., Frenk C. S., 1991, *MNRAS*, **249**, 662
- Pritchard J. R., Loeb A., 2012, *Reports on Progress in Physics*, **75**, 086901
- Qin Y., Wyithe J. S. B., Oesch P. A., Illingworth G. D., Leonova E., Mutch S. J., Naidu R. P., 2022, *MNRAS*, **510**, 3858
- Richard J., et al., 2007, *ApJ*, **662**, 781
- Saha P., Sluse D., Wagner J., Williams L. L. R., 2024, *Space Sci. Rev.*, **220**, 12
- Schneider P., Ehlers J., Falco E. E., 1992, *Gravitational Lenses*, [doi:10.1007/978-3-662-03758-4](https://doi.org/10.1007/978-3-662-03758-4).
- Sharon K., et al., 2020a, *ApJS*, **247**, 12
- Sharon K., et al., 2020b, *The Astrophysical Journal Supplement Series*, **247**, 12
- Shimabukuro H., Mao Y., Tan J., 2022, *Research in Astronomy and Astrophysics*, **22**, 035027
- Silva M. B., et al., 2021, *Experimental Astronomy*, **51**, 1593–1622
- Sobacchi E., Mesinger A., 2014, *MNRAS*, **440**, 1662
- Stark D. P., 2016, *ARA&A*, **54**, 761
- Suto D., Kitayama T., Nishimichi T., Sasaki S., Suto Y., 2016, *Publications of the Astronomical Society of Japan*, **68**
- Tang M., et al., 2023, JWST/NIRSpec Spectroscopy of  $z = 7 - 9$  Star Forming Galaxies with CEERS: New Insight into Bright Ly $\alpha$  Emit-

- ters in Ionized Bubbles ([arXiv:2301.07072](https://arxiv.org/abs/2301.07072)), <https://arxiv.org/abs/2301.07072>
- Tashiro H., Sugiyama N., 2012, *MNRAS*, **420**, 441
- Tilvi V., et al., 2020a, *ApJ*, **891**, L10
- Tilvi V., et al., 2020b, *The Astrophysical Journal Letters*, **891**, L10
- Tingay S. J., et al., 2013, *Publ. Astron. Soc. Australia*, **30**, e007
- Tinker J., Kravtsov A. V., Klypin A., Abazajian K., Warren M., Yepes G., Gottlöber S., Holz D. E., 2008, *ApJ*, **688**, 709
- Trapp A. C., Furlanetto S. R., Davies F. B., 2023, *MNRAS*, **524**, 5891
- Turner E. L., 1980, *ApJ*, **242**, L135
- Venditti A., Bromm V., Finkelstein S. L., Graziani L., Schneider R., 2024, *MNRAS*, **527**, 5102
- Wambsgans J., 1998, *Living Reviews in Relativity*, **1**, 12
- Watson D., Christensen L., Knudsen K. K., Richard J., Gallazzi A., Michałowski M. J., 2015, *Nature*, **519**, 327
- Wyithe J. S. B., 2004, *MNRAS*, **351**, 1266
- Wyithe J. S. B., Loeb A., 2004, *Nature*, **432**, 194
- Xu H., Norman M. L., O’Shea B. W., Wise J. H., 2016, *ApJ*, **823**, 140
- Yoshida N., Omukai K., Hernquist L., Abel T., 2006, *ApJ*, **652**, 6
- Yoshiura S., et al., 2021, *MNRAS*, **505**, 4775
- Zahn O., Lidz A., McQuinn M., Dutta S., Hernquist L., Zaldarriaga M., Furlanetto S. R., 2007, *ApJ*, **654**, 12
- Zheng Q., Wu X.-P., Johnston-Hollitt M., Hua Gu J., Xu H., 2016, *The Astrophysical Journal*, **832**, 190
- van Haarlem M. P., et al., 2013, *A&A*, **556**, A2
- von Wietersheim Kramsta M., et al., 2021, *Monthly Notices of the Royal Astronomical Society*, **504**, 1452–1465
- Árdís Elíasdóttir et al., 2007, Where is the matter in the Merging Cluster Abell 2218? ([arXiv:0710.5636](https://arxiv.org/abs/0710.5636)), <https://arxiv.org/abs/0710.5636>

This paper has been typeset from a  $\text{\TeX}/\text{\LaTeX}$  file prepared by the author.